PERGAMON

Deep-Sea Research II 49 (2002) 1253–1277

DEEP-SEA RESEARCH
PART II

www.elsevier.com/locate/dsr2

A numerical study of the Somali coastal undercurrents

O.E. Esenkov[a,*], D.B. Olson[b]

[a] *Cooperative Institute for Marine and Atmospheric Studies, University of Miami, FL, USA*
[b] *Rosenstiel School of Marine and Atmospheric Science, University of Miami, FL, USA*

Accepted 22 September 2001

Abstract

Subsurface circulation in the western Arabian Sea is studied with an open boundary version of the Miami Isopycnic Coordinate Ocean Model (MICOM). The model solution demonstrates a strong annual cycle and significant alongshore variability of subsurface circulation. Based on the dynamics and water properties, three regions are identified along the coast.

A cross-equatorial current, which exists throughout the year, carries low-salinity water northwards. Comparison of the model results with observations in the equatorial region demonstrates that the model reproduces the annual cycle and transport of the currents remarkably well. Although it underestimates the speed of the undercurrent core by about a factor of two, increasing the horizontal resolution from 0.35° to 0.225° improves agreement with the measurements. A spring southward undercurrent between 5°N and the equator owes its existence to the wind forcing in the Arabian Sea.

Water with higher salinity values, found in the coastal region north of 5°N, is advected by a southward undercurrent that is present between October and March. The existence of the undercurrent is caused by flows from the east and northeast. The latter originates in the Persian Gulf and provides about 75% of water for the coastal undercurrent. The annual Rossby wave generated in the interior of the domain contributes to the formation of the current in the fall. The third region is an area near 4°N, where the southward undercurrent separates, as velocity and salinity fields suggest. Subsurface circulation north of 5°N is disconnected from flows near the equator during most of the year.

The model circulation is not sensitive to the details of coastal bottom topography. In contrast, the presence of the Socotra Island, which is absent in the model, leads to a more realistic solution in that the southward undercurrent north of 5°N is present throughout the spring. Interannual variability of the model subsurface fields increases significantly when observed, rather than climatological, wind forcing is used. The most dramatic changes occur in the coastal and equatorial regions.

1. Introduction

The annual oceanic transport of heat is southward in the Indian Ocean. While advection of surface water occurs in the interior of the ocean, observations (Godfrey et al., 1995) and solutions of General Circulation Models (McCreary et al., 1993, later referred to as MKM; Wacongne and Pacanowski, 1995) demonstrate that subsurface replacement is through western boundary currents within the thermocline.

Cross-equatorial transport of low-salinity water below the surface may have a strong impact on the

*Corresponding author. 1615 Hermann Drive Unit 1209, Houston, TX 77004-7147, USA.

E-mail address: esenkov@aoml.noaa.gov, esenkov@hotmail.com (O.E. Esenkov).

0967-0645/02/$ - see front matter
PII: S0967-0645(01)00152-7

near-surface salt budget in the region, as analysis by the authors of this paper (not presented here) suggests. Some of the subsurface water supplied by coastal undercurrents from the Southern Hemisphere participates in strong coastal upwelling off the Somali coast during summer. Quadfasel and Schott (1983, later referred to as QS) infer vertical velocities as high as 6×10^{-3} cm/s at 130 m depth near 6–8°N. The upwelled cold water is subsequently advected by two strong gyres offshore, modifying surface heat flux over relatively large areas of the Arabian Sea. In addition, upwelling conditions lead to a very productive biological response in the form of intense, long-lasting phytoplankton blooms in the northwestern Arabian Sea (Brock and McClain, 1992; McCreary et al., 1996). Therefore, knowledge of the annual cycle and variability of circulation and water-mass properties below the surface can provide a better understanding of ecosystem dynamics, ocean heat and salt budgets in the Arabian Sea, and, possibly, monsoon variability (Shukla, 1987).

While surface circulation in the northern Indian Ocean has been studied extensively over more than three decades, available hydrographic data set is particularly sparse in the Indian Ocean. It consists of shipboard measurements within a few months of a particular year, and long-time mooring measurements at one point. As a result, characteristics and annual cycle of subsurface circulation are not well known. In this study evolution of subsurface fields off the coast of Africa is examined with an isopycnic-coordinate numerical model. First, results of the model are compared with available observations. Model subsurface circulation is then analyzed in detail. Effects of bottom topography and variable wind forcing on the evolution of the coastal undercurrents are addressed in the subsequent sections.

1.1. Observational background

The Somali Current, with a volume transport comparable to that of the Gulf Stream, changes direction with the monsoon winds. It flows northeastward during the summer and southwestward in the winter (Fig. 1). Below the Somali Current, coastal undercurrents with strong alongshore and seasonal variability are observed (QS; Schott, 1983, later referred to as S83). The annual cycle of coastal subsurface circulation sketched in Fig. 2 was inferred from measurements near 4°S (Duing and Schott, 1978), at the equator (Schott et al., 1990, later referred to as SSF), and between 5°N

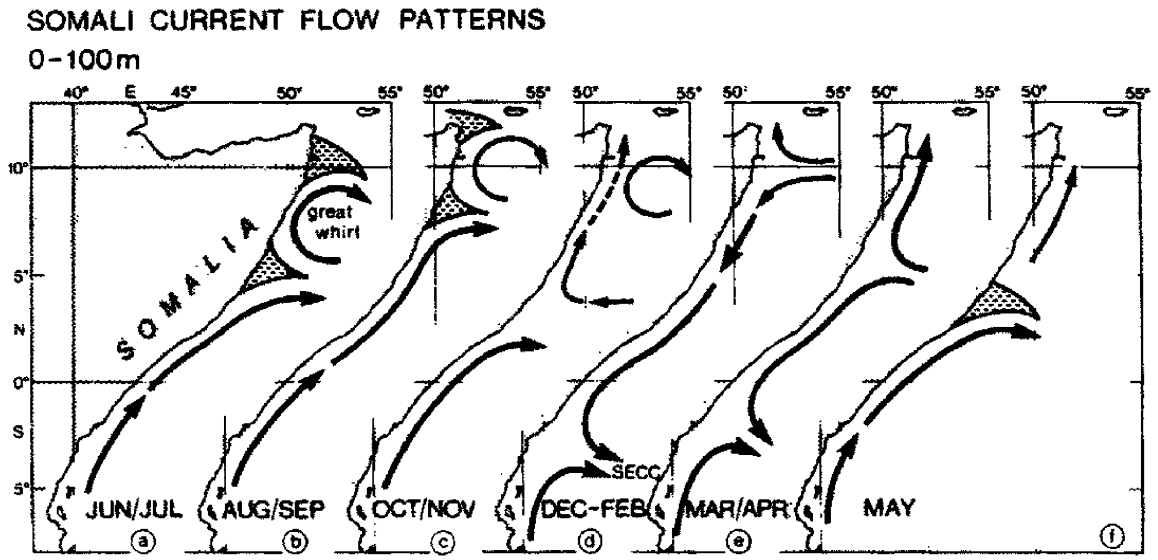

Fig. 1. Schematic representation of coastal currents off Somali at the surface. Shaded regions represent wedges of upwelled water.

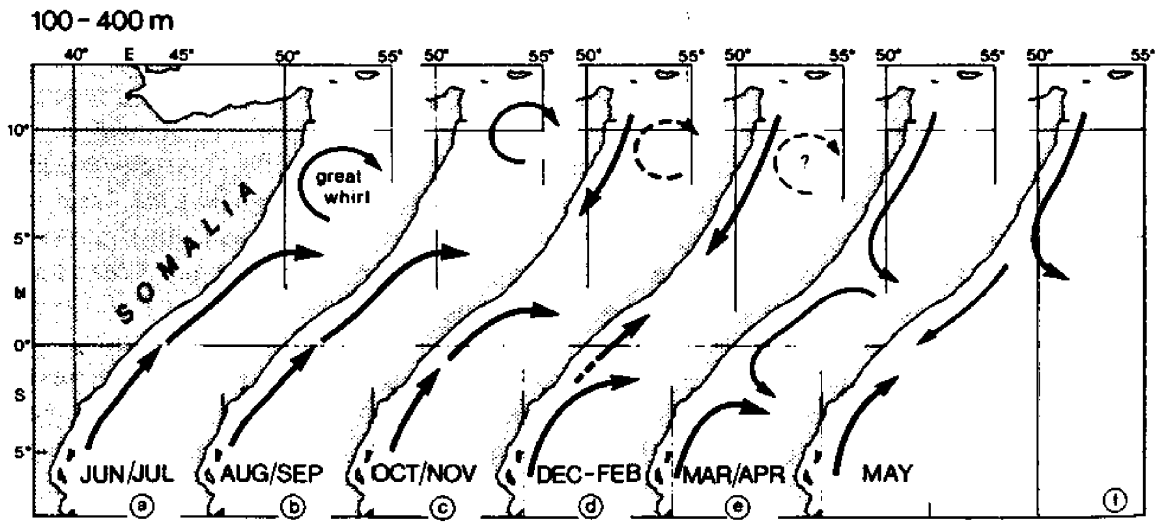

Fig. 2. Schematic representation of coastal currents off Somalia at 100–400 m depth range (from Schott et al., 1990). Note that the figure is based on observations at several locations alongshore during different years and on analysis of distribution of properties.

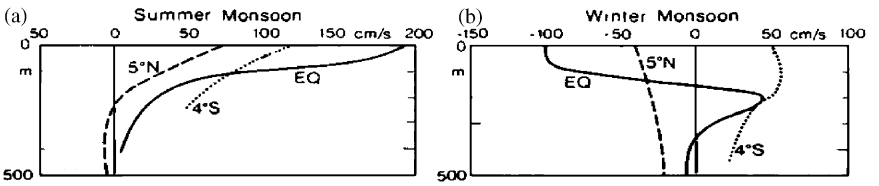

Fig. 3. Current profiles at 4S (after Duing and Schott, 1978), on the equator (after Schott et al., 1990) and at 5°N (after QS) (a) for summer monsoon, (b) for winter monsoon (from Schott et al., 1990). Note that averaging periods are not the same for the three profiles.

and 9°N (QS). Current profiler sections taken in the last region between October and May show a subsurface southward flow about 50–100 km wide. The undercurrent occupies a depth range between 150 and 600 m at 9°N and its core, found in the range 300–400 m in this location, rises in the downstream direction to 200–300 m near 5°N. The maximum speed increases from 15 to 60 cm/s. The current shows strong seasonal variability in phase with the near-surface flow, suggesting a close coupling to the monsoonal wind forcing. Relative vorticity in the undercurrent is found to increase by the same amount as the decrease of the Coriolis parameter between these latitudes implying conservation of potential vorticity. The current is not detected at 3°N, which led Schott (1983) to suggest that it separates from the coast between 5°N and 3°N. The undercurrent between 10°N and 5°N disappears after the onset of the summer monsoon and formation of a deep anticyclonic Great Whirl in this region.

Observations near the equator suggest that circulation there is disconnected from the undercurrent farther north during most of the year (SSF). Both surface and deeper circulations reveal a strong seasonal cycle (Fig. 3). While the Somali Current decays monotonically in the vertical during the summer monsoon, no deep-reaching boundary current exists during the winter. Rather, there are southward flows above and below a northward current in the 120–400 m depth range, which are not connected to the monotonically

decaying southward boundary current farther north. Based on the observed behavior and characteristics of the subsurface flows, three regions can be identified alongshore (Figs. 3 and 2): (i) between 10°N and 5°N, where a continuous southward flow is observed during October–May; (ii) near the equator, where circulation seems to be disconnected from flows farther north and a southward undercurrent is present between 5°N and the equator in spring; (iii) around 4°N where separation of the southward undercurrent is expected. Investigation of annual cycles and characteristics of the model currents in these regions is the focus of this study.

1.2. Modeling background

Different mechanisms of generation and decay of the coastal undercurrent have been proposed in the past. An undercurrent in a two-layer flat bottom numerical model of Hurlburt and Thompson (1976) does not agree with observations in that it exists during the Southwest Monsoon as a cyclonic outflow in the lower layer of the Great Whirl. Using a linear, continuously stratified model with vertical and horizontal mixing, McCreary and Kundu (1985) demonstrated that no undercurrent develops in response to alongshore winds at a western boundary and that remote forcing is required for its existence. A strong onshore current, located near the southern edge of the wind field, is generated by an offshore wind curl in their study. Part of this current turns southward at the coast, thereby generating the undercurrent in the south. In contrast to this, a $2\frac{1}{2}$-layer model of McCreary and Kundu (1988) developed no undercurrent for winds even with a non-zero stress curl. The authors suggested that strong entrainment, which requires a continuous source of the lower layer water, or the simplicity of the wind forcing used, could be responsible for inability of the model to produce the coastal undercurrent.

Jensen (1991) concluded that equatorial onshore flow below the thermocline in a $3\frac{1}{2}$-layer model is associated with the disappearance of the undercurrent below the Somali Current in June and that its return is caused by baroclinic instability of the Great Whirl followed by a reversal of equatorial undercurrents in the fall. Jensen (1991) suggested that remote winds control the intermediate depth flow along the Somali coast acting through Rossby waves generated along the west coast of India.

MKM describe three coastal undercurrents present in their solution. An undercurrent present from October through February is a result of forcing during the previous Southwest Monsoon. A band of higher upper-layer thickness, which was generated by Ekman pumping during the summer, propagates westward as a Rossby wave with the weakening of the winds. The southward subsurface flow near the coast is associated with a mode-2 response. The separation latitude of the undercurrent (near 3°N) is thus largely determined by the wind pattern off the Somali coast during the previous Southwest Monsoon. A spring undercurrent present south of 5°N is primarily remotely forced by Rossby waves that had radiated from the coast of India. The third undercurrent in MKM solution is a cross-equatorial coastal flow that penetrates as far as 2.5°N and lasts through February. The authors suggest that the main cause of this current is the inertial overshoot of the western-boundary current.

2. Description of a numerical model

Significant progress in the understanding of processes governing the evolution of subsurface circulation off Somalia has been made with the reduced-gravity models described above. The models, however, had a low resolution in the vertical and lacked some physical processes, such as interaction of the boundary current with the bottom topography, which has been suggested to have a strong effect on the undercurrent behavior (S83). An isopycnic coordinate model, used in this study, avoids these limitations. General description of the Miami Isopycnic Coordinate Ocean Model (MICOM) can be found in Bleck et al. (1992) and references therein. An important feature of the model for studying the upwelling region off Somalia is its ability to reduce the vertical truncation error by concentrating coordinate surfaces in regions with large vertical and

horizontal density gradients. Also, effects of numerically induced mixing are avoided by formulating the equations in isopycnic coordinates. The model thermodynamically active mixed layer of Kraus and Turner (1967) type lies on top of a stack of isopycnic layers. MICOM includes entrainment and detrainment into the mixed layer, and can handle the difficulties associated with isopycnic layers outcropping or running into the bottom.

A regional version of MICOM is used in this study. Its advantage is that it allows us to perform simulations in a reasonably accurate and computationally inexpensive way compared to the cost of running the global MICOM. Initial and boundary conditions for an open-boundary version of the MICOM used in this study (Bleck, personal communication) are formulated using output from the global model run. Well-posed boundary conditions derived from the theory of characteristics (Browning and Kreiss, 1982, 1986) are applied to the barotropic mode. The model has 16 layers and occupies a region between 4°S and 23°N, and 40°E and 68°E (Fig. 4), with 0.35° horizontal resolution (one run with 0.225° resolution has been performed and is discussed in this study). The vertical structure of the upper thermocline is reasonably well resolved with seven layers in the upper 400 m. Bottom topography was obtained by interpolating the ETOPO5 data set to the model grid points. This resulted in a reasonably good representation of bathymetry except that the Socotra Island is submerged under about 300 m of water. Possible effects of this deficiency on the model results are examined in a run with an artificially restored island.

If not stated otherwise, both wind and thermodynamic climatological forcing are used. Precipitation data were obtained by the special sensor microwave/imager (SSM/I), while the Comprehensive Ocean-Atmosphere Data Set (COADS) data set is used for the other forcing fields.

The open-boundary model was validated first through a detailed comparison of the results with the output of the global model. The analysis shows that both models similarly reproduce the major observed features of circulation in the region, with correct timing and geographical locations of the events. Some noticeable differences are observed, however, in a small region off Somalia where intense eddies form during the summer monsoon.

3. Model results

3.1. Annual cycle of circulation below the surface

Model circulation between approximately 200 and 300 m flow pattern includes several eddies near the Somali coast in January (Fig. 4a). A southward undercurrent between 10°N and 5°N exists both in the model solutions and in the observations during winter (cf. Figs. 4a and 2d; see also Figs. 10a and b). The undercurrent is about 85 km wide, and its velocity reaches 20–30 cm/s. A northward cross-equatorial flow is very weak at this time. During the spring transition a southward undercurrent south of 6°N turns offshore near 2°S (Figs. 4b and 2e). The undercurrent north of 6°N is not well developed at this time, and even regions of northward flow appear in this region. Model subsurface circulation in the summer qualitatively resembles the observations (Figs. 4c and 2a). The two strong, deep-reaching eddies dominate circulation in the region. Remnants of the summer Great Whirl still determine flow patterns in the northern part of the Somali coastal region in the fall in the model (Fig. 4d), while the observations suggest that the eddy is separated from the coast by a southward undercurrent at this time (Fig. 2c). While the model and observed circulations are in general agreement in the coastal region off Somalia during most of the year, some differences occur in spring when the undercurrent north of 6°N does not exist in the model. Zonal onshore flow accounts for the appearance of the southward undercurrent south of this latitude. This flow is caused by propagation of a Rossby wave that forms in the Arabian Sea during the intermonsoonal transition.

Evolution of the alongshore transport between 50 and 300 m near the western boundary is presented in Fig. 5. The southward undercurrent north of 5°N appears in October, and its transport increases through the rest of the winter monsoon.

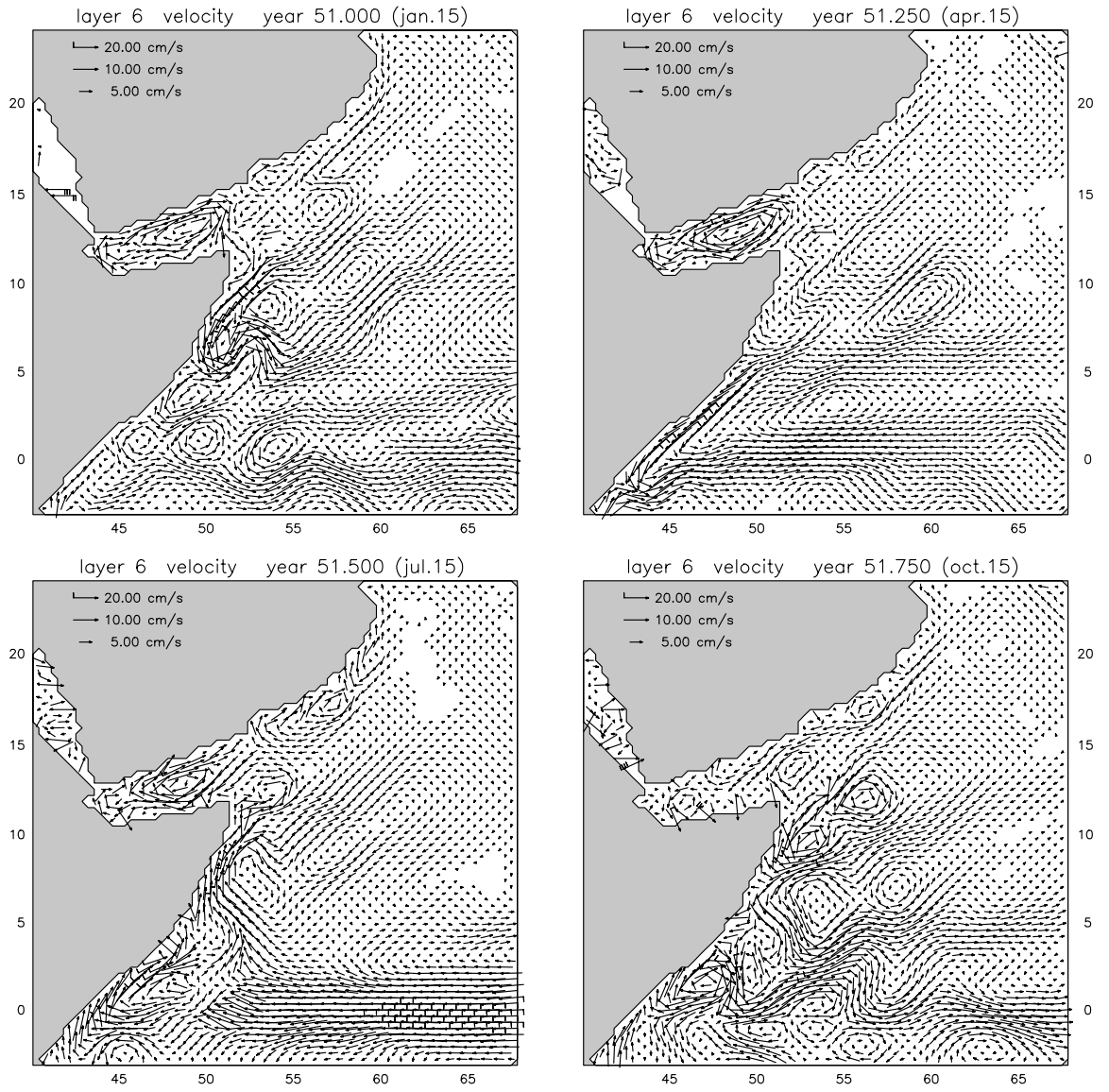

Fig. 4. Seasonal cycle of model circulation in the depth range between 220–250 m and 320–350 m. Barbed arrows correspond to current speed of 20 cm/s. A southward coastal undercurrent is not present during the summer monsoon.

While the largest transport values are found north of 5°N, a weak southward flow exists as far south as 3°N. South of this latitude propagation of the undercurrent seems to be blocked by a northward cross-equatorial flow. The latter weakens after December, while the southward undercurrent is still confined to north of 5°N. Transport in the coastal region is still southward during March, and changes sign in mid-April. Negative transport values south of 5°N during March–May correspond to the southward undercurrent, which also has been observed at this time (Fig. 2). Northward flow in this region strengthens significantly during the summer, especially when the Great Whirl

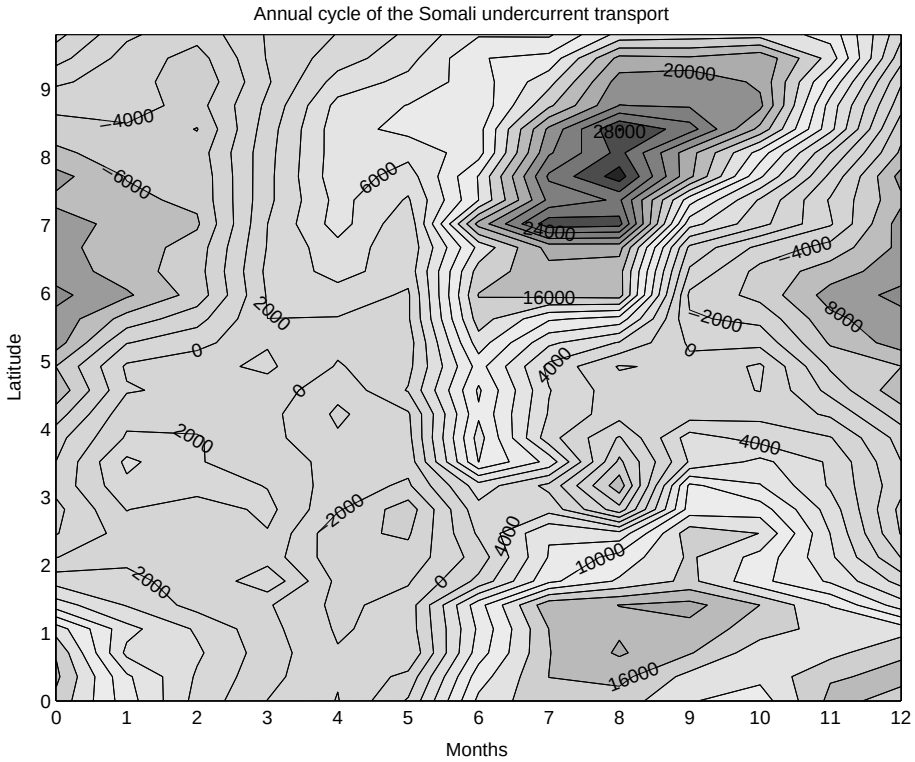

Fig. 5. Annual cycle of transport near the coast in depth range between 50 and 300–350 m. A southward undercurrent north of 5°N appears in October and lasts through March in the standard run.

forms in late June. Another region of strong northward flow appears south of 2–3°N when the East African Coastal Current crosses the equator.

Because observations of subsurface circulation in the western equatorial region are one of the most complete in the Arabian Sea (SSF), the model transport is compared with measurements here. Strong seasonal variability of the model cross-equatorial transport in the upper 500 m is evident in Fig. 6. The model mean transports of 0.7 and 23.3 Sv for winter and summer monsoons, respectively, compare favorably with observed values of 0 and 21 Sv for the corresponding monsoons (SSF). The agreement is even better for annual means: 9.97 Sv in the model and 10 Sv in the observations. The model underestimates, however, velocities in the core of the undercurrent by about a factor of two in winter (27 vs 50 cm/s, cf. with Fig. 3). This deficiency can be attributed to some extent to insufficient horizontal resolution in the western boundary region. When horizontal resolution is increased from 0.35° to 0.225° (Fig. 7), maximum velocity reaches 52 cm/s, which is closer to the measured value but occurs at a lower depth (near 100 m).

4. Evolution of subsurface properties

Measurements of salinity in the coastal zone off Somalia in winter and spring show that the region of high-salinity values, bounded by a sharp front from the low-salinity Subtropical Subsurface Water farther offshore, is well correlated with the core of the undercurrent (QS, their Fig. 7). Characteristics of the coastal undercurrent north of 5°N thus may be important for salinity budget in the Arabian Sea.

The shape of the model isohaline contours in the coastal region is in qualitative agreement with the

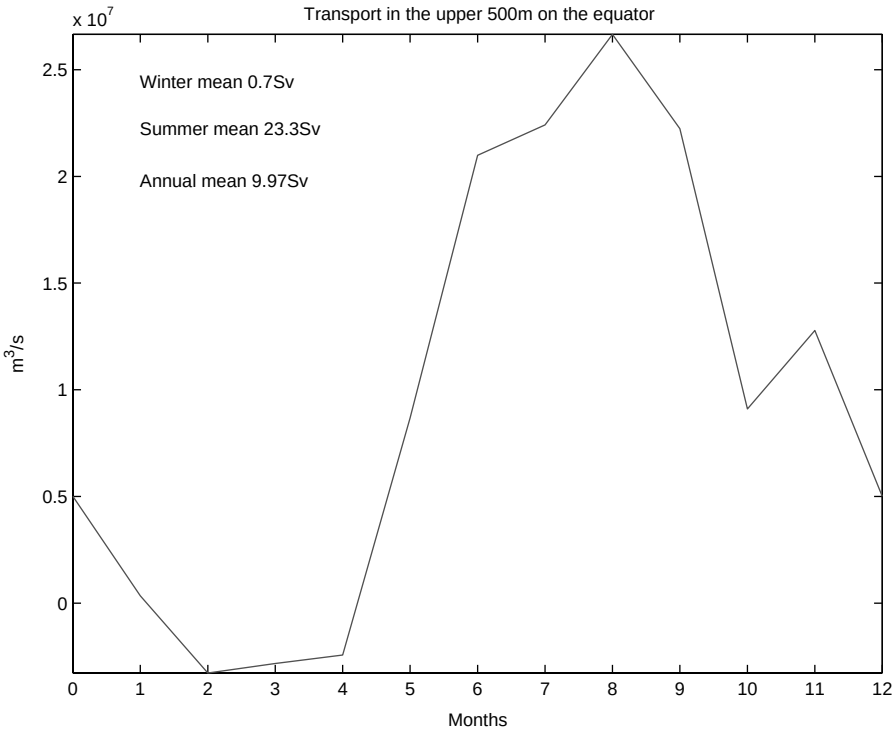

Fig. 6. Seasonal cycle of cross-equatorial transport in the upper 500 m near the western boundary. Seasonal and annual means of the model transport compare favorably with measurements of 0 Sv and in winter, 21 Sv in summer, and 10 Sv on annual mean.

observed fields. The model salinity values in the undercurrent depth range differ only by about 0.1 psu from the observations (QS). The highest salinity values in the model found near the coast between 200 and 400 m north of 5°N demonstrate that the coastal undercurrent advects high-salinity water southwards in the winter (Fig. 8a), in general agreement with the measurements. However, the distribution of salinity in the model shows less variability in the zonal direction. South of 5°N (Fig. 8b), salinity increases in the offshore direction in this depth range, suggesting that a northward coastal flow carries relatively low-salinity equatorial water. It will be shown in a subsequent paper that this low-salinity water plays an important role in the salinity budget of the Arabian Sea. Some of this water participates in the summer upwelling at the Somali coast.

A high-salinity wedge in the salinity field vertically averaged over the depth range 150–450 m in May supports the idea of the near-equatorial turnoff of the undercurrent (Fig. 8 in QS). As in the observations, salinity distribution in the model shows signs of the flow separation near 5°N in winter, when the undercurrent is the strongest. Fig. 9a demonstrates advection of salinity contours in the nearshore zone by a southward undercurrent. A region of stagnation is found near 5°N where a salinity front forms in January. The frontal structure further intensifies in February (Fig. 9b) due to alongshore salinity advection from the north. The salinity gradient starts decreasing in April, when the southward coastal undercurrent loses intensity. It is clear from these plots that some mechanism prevents penetration of high-salinity water southwards and is likely associated with the undercurrent separation in this region. To summarize, salinity field in the subsurface layers presents additional evidence of separation of the southward coastal undercurrent near 5°N. The undercurrent advects high-salinity water equatorward while a northward current south of

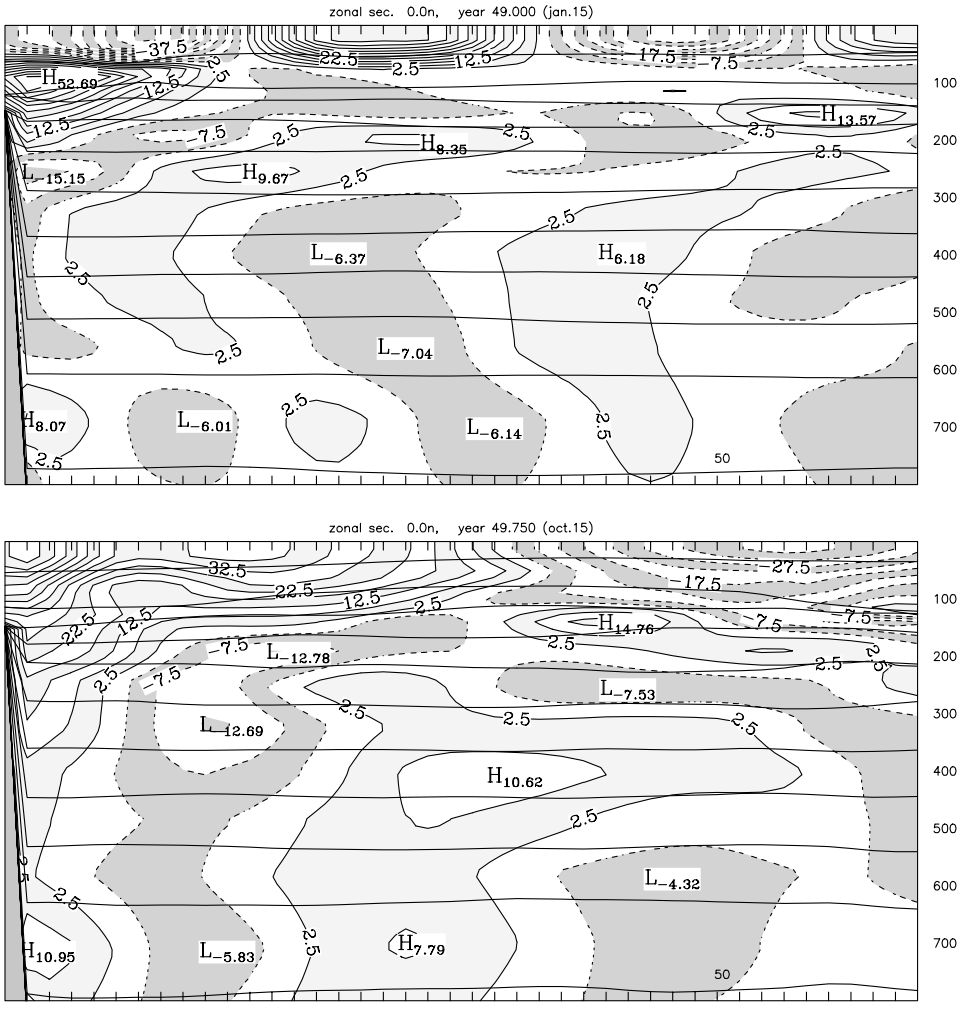

Fig. 7. Cross-equatorial currents in MICOM with horizontal resolution increased from 0.35° to 0.225° in winter and fall. The highest velocities in the undercurrent core are about a factor of 2 larger than those in the standard run in January. Lighter shading corresponds to regions of northward flows, darker shading to southward flows. Solid lines represent interfaces between the model layers. Tick marks on the horizontal axis correspond to locations of the model's grid points.

5°N is responsible for appearance of water with lower salinity in the coastal region.

4.1. Vertical structure of coastal circulation north of 5°N

A time series of the vertical structure of the model coastal circulation at several locations north of 5°N is shown in Figs. 10a–c. Winter flow near 8.4°N is northward in the upper 180 m, while it is in the opposite direction below, with velocity reaching 15 cm/s near 260 m (Fig. 10a). The northward surface flow is opposite to the observed current (see Fig. 1) because of the wind stress distribution used in the model, as analysis in Section 5 shows. The southward undercurrent accelerates and its core rises in the downstream direction. It is below 100 m at 7°N, with a maximum of 20 cm/s near 280 m (Fig. 10b). At 5.3°N the flow is southward in the upper 600 m, with the highest velocities near the surface (Fig. 10c). The surface northward current

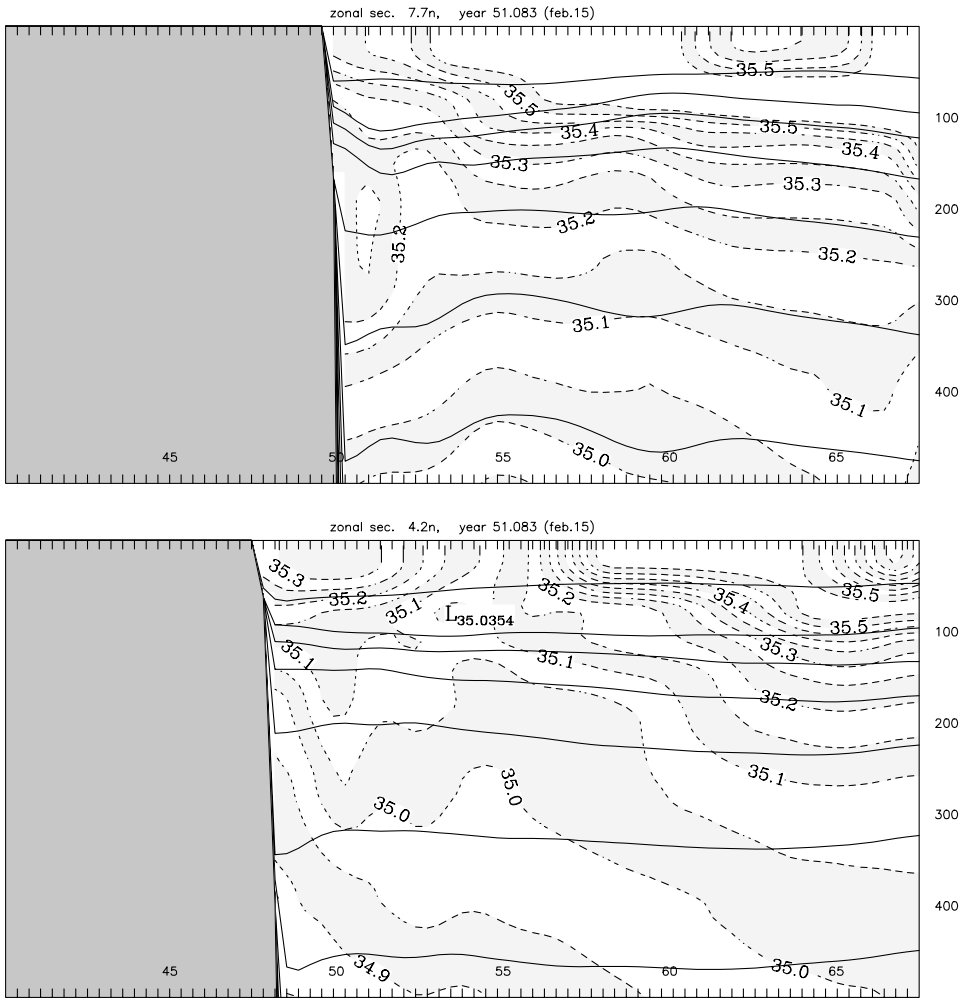

Fig. 8. Salinity cross-sections at 7.7°N (a) and 4.2°N (b) in February. Solid lines represent interfaces between the model layers. Shading corresponds to regions with different salinity values. Note subsurface water with higher than ambient salinity at 7.7°N. Salinity distribution is reversed at 4.2°N. Solid lines represent interfaces between the model layers. Tick marks on the horizontal axis correspond to locations of the model's grid points.

intensifies and deepens in March and April, while the southward flow underneath it weakens considerably. The latter reverses, and a northward flow is found in the upper 800 m near 8.4°N and 7°N in May. A southward undercurrent is still present at 5.3°N at this time. Summer circulation looks qualitatively similar at all three locations due to a strong northward flow near the coast in the Great Whirl, with the highest velocities near the surface. The flow is still northward at 8.4°N in September when equatorward currents appear below 550 m farther south. The southward current strengthens and is found below 150, 200, and 600 m at 5.3°N, 7°N, and 8.4°N, respectively, under a northward near-surface current in October. The latter weakens during the winter monsoon, when the southward flow underneath it intensifies. The undercurrent rises on the way south and is found below 150 m at 8.4°N, below 100 m at 7°N and at the surface at 5.3°N in December. While the annual cycle, horizontal and vertical extent of the model undercurrent north of

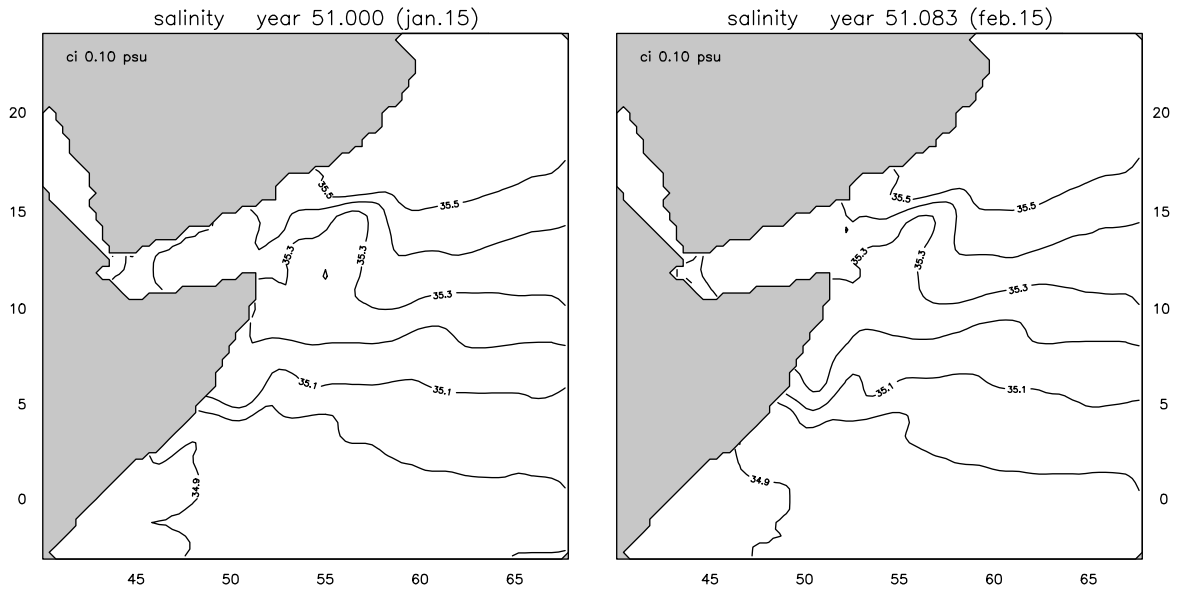

Fig. 9. Evolution of the model salinity distribution in the depth range between 200 and 300 m in winter. Formation of salinity front near 5°N is evident in the figure.

5°N are in general agreement with the available observations, measured velocities are higher (by as much as a factor of 2) than those in the model. This discrepancy to a certain degree can be attributed to a limited horizontal and vertical resolution and climatological wind forcing used in the model.

4.2. Evolution of coastal undercurrents at the equator

Observations suggest that equatorial circulation near the western boundary of the Indian Ocean is disconnected from flows farther north during most of the year (Schott, 1986). Mooring array measurements at the equator show very strong seasonal variability of subsurface circulation. A deep-reaching northward flow during the summer is replaced by vertically reversing currents in the winter. Very little transport is measured at higher depths, between 500 and 1000 m, during either season (SSF).

Evolution of the near-equatorial circulation in the model is shown in Fig. 10e. A northward current between 75 and 300 m reaches 27 cm/s in January. Southward flows are found above and below it, with largest velocities near the surface. The vertical extent of the northward undercurrent decreases in February and March when it is found between 70 and 230 m, while the southward flow below it intensifies. A rather weak northward flow occupies the upper 170 m in April, with the core located near 120 m. The current strengthens with near-surface velocities exceeding 90 cm/s in May, after a full development of the Southern Gyre. The northward current, which reverses near 150 m at this time, subsequently deepens to 250 and 450 m in June and July, respectively, and the southward flow underneath it disappears. During the fall transition between the monsoons a northward flow is present in the upper 800 m near the coast. The highest near-surface velocities decrease from the summer values to 60–70 cm/s at this time. This distribution of velocity changes in December when a weak southward flow replaces the northward current in the upper 50 m. A northward current below it reaches 40 cm/s at this time, and the described cycle is repeated. This analysis demonstrates that annual cycle of the model circulation on the equator is in general agreement with measurements and transport calculations.

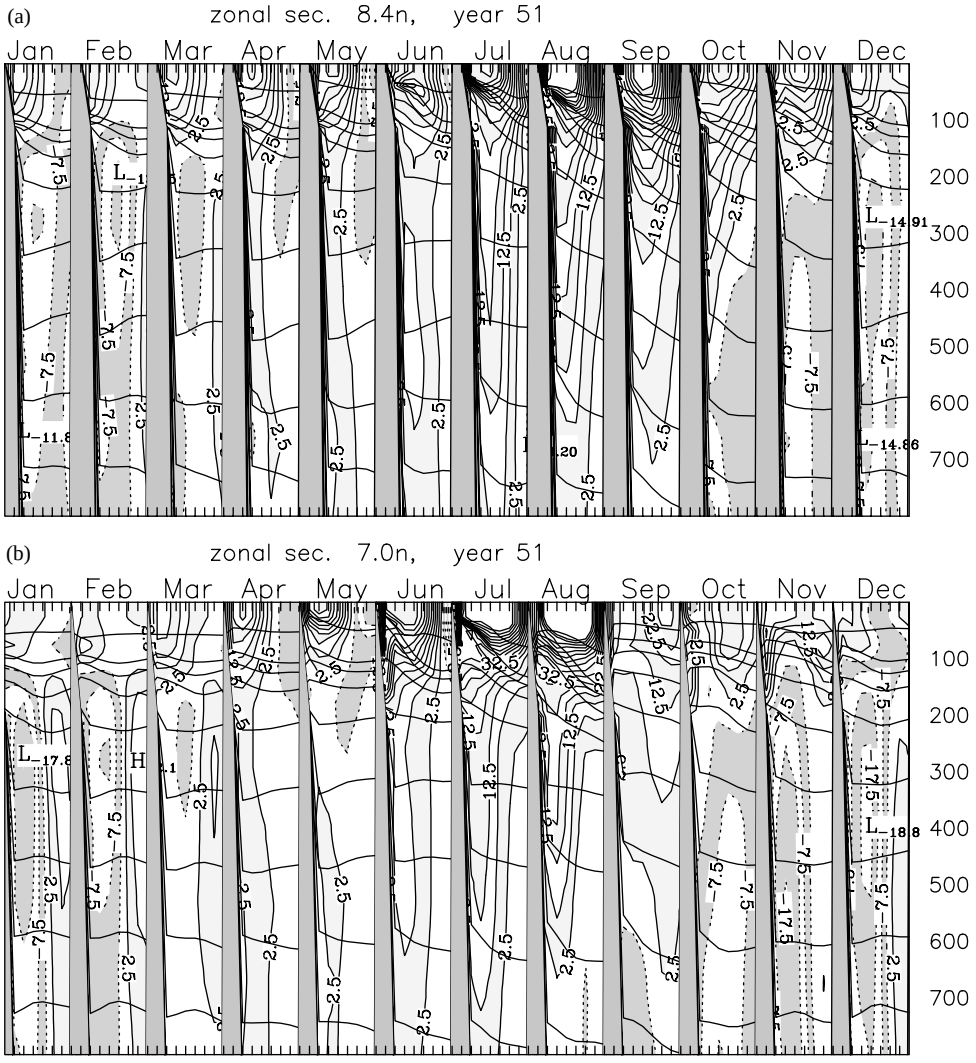

Fig. 10. Time series of the model alongshore flows (a) at 8.4N, (b) at 7N, (c) at 5.3N, (d) at 3.5N, and (e) on the equator. Horizontal scale is about 39 km. Each section is approximately 273 km long. Contour interval is 5 cm/s, zero contour is suppressed. Lighter shading corresponds to regions of northward flows, darker shading to southward flows.

Another undercurrent forms between about 5°N and the equator (Figs. 10d and e), in qualitative agreement with the observations and results of MKM. In the latter, this undercurrent appears to be primarily remotely forced by Rossby waves that had radiated from the west coast of India. In the current solution, it is caused by propagation of waves formed as a result of the abating winter monsoon winds in the Arabian Sea.

4.3. Annual cycle of circulation near 4°N

There is no southward undercurrent in the model in the depth range between 200 and 300 m near 4°N in winter (Fig. 4a). A southward coastal flow meets a northward current in this region and both currents turn offshore. Collision of the undercurrents, however, cannot fully explain the separation, because the flow from the north is

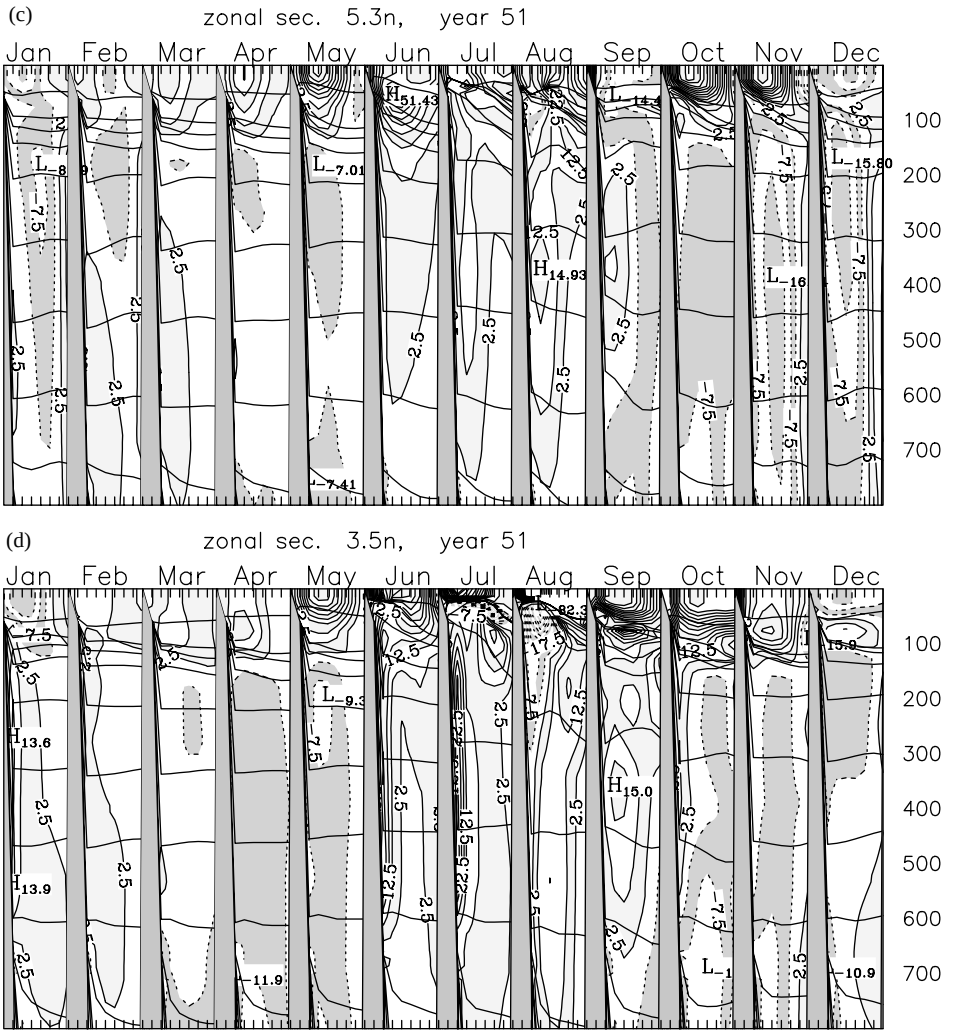

Fig. 10. (*Continued*)

stronger than the opposing current. A southward undercurrent appears in this region only during the spring transition period as a result of a strong onshore flow near 5°N (Fig. 4b). During the rest of the year, coastal flow is either northward or very weak southward.

A time series of the vertical structure of the nearshore flow in the upper 800 m clearly demonstrates that while there exists a strong southward undercurrent at 5.3°N in January and February (Fig. 10c), the flow is in the opposite direction in this depth range at 3.5°N (Fig. 10d). Only in April and May a southward current appears south of 4°N. The undercurrent at 3.5°N is significantly weaker than that at 5.3°N in October and November, and its core is found farther offshore, suggesting a separation in this region. Differences between flows in these locations become even more pronounced later in the winter monsoon. While the current intensifies and its core rises with time at 5.3°N and at locations farther north, flow south of 4°N remains weak. Thus, the subsurface circulation near 4°N differs from currents north and south of this region. Mechanisms responsible for

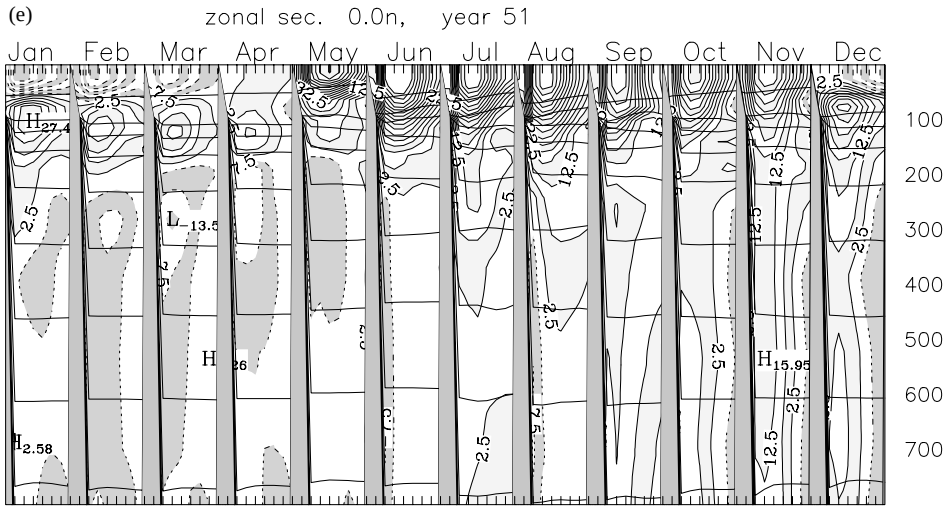

Fig. 10. (*Continued*)

the described changes of the subsurface flow on its way south remain unclear. As suggested by Schott (1983), effects of topography and change to the equatorial dynamics in the region near 4°N could be responsible for the undercurrent separation, and are addressed below.

5. Formation of the winter undercurrent north of 5°N

Unlike undercurrents in upwelling regimes, which exist as a dynamic response to modifications of density field near the coast, the Somali undercurrent north of 5°N occurs during the Northeast Monsoon, when winds lead to coastal downwelling. The goal here is to establish mechanisms responsible for the existence of the undercurrent.

5.1. Connection to offshore currents

Recent observations by Schott and Fischer (2000) show that a zonal surface flow between 8°N and 10°N, caused by the wind distribution in this region, splits at the coast in winter. The southward branch constitutes the winter Somali Current. Part of the northward branch flows between the tip of Somalia and Socotra Island, while the rest recirculates south of the island (Fig. 11). Subsurface circulation (between 100 and 700 m) is in the same direction as the Somali Current south of about 9°N, while it is in the opposite to the surface flow direction north of this latitude (Fig. 11b). For the ease of discussion we call the extension of subsurface flow south of 9°N an undercurrent, even though it is a part of a surface southward current. Flows from the north and east feed the southward undercurrent at this time.

The model surface circulation in the region north of 5°N (top left panel in Fig. 12) agrees with the observations by Schott and Fischer (2000). A zonal inflow follows the zero wind-stress curl line, in accordance with the circulation system adjusting toward Sverdrup balance. A westward current bifurcates at the coast but about 1 degree farther south than in reality. Some of the northern branch water continues northward, while the rest turns northeastward south of a region where the Socotra Island should be present. Subsurface circulation in the model is more complicated than that inferred from the observations (Fig. 11b), and includes several eddies along the coast. There is a southward flow through the Socotra passage in winter. A subsurface anticyclone centered near 10°N is possibly a remainder of the summer Great Whirl (top right panel in Fig. 12). There is a deep inflow from the northeast, while a southward current through the passage is rather shallow. The latter is confined to depths between 150 and 250 m, which

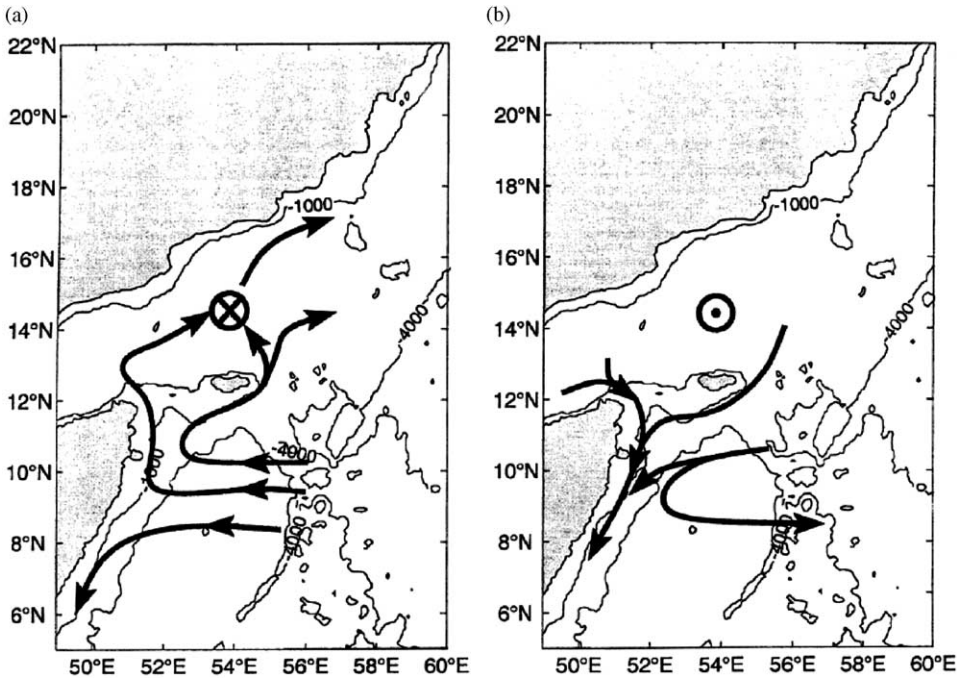

Fig. 11. Circulation patterns (a) at the surface, (b) in the 100–700 m depth range, inferred from observations by Schott and Fischer (2000). The southward undercurrent off Somalia is supplied by water from the north and northeast.

correspond to the fifth layer in the model (bottom left panel in Fig. 12). To estimate contributions from both currents to the coastal undercurrent, transports from the north and from the east were calculated (Fig. 13). Transport values are always negative in the figure because only the southward and the westward components, which contribute to the southward coastal undercurrent, are taken into account for simplicity. Flow from the east dominates during the winter monsoon, when the undercurrent north of 5°N is strongest. About a quarter of the water for the undercurrent comes from the north, while the rest is provided by the flow from the east.

A careful inspection of Fig. 4a and results of the global MICOM (R. Bleck, personal comm.) shows that the northeastward flow originates in the Persian Gulf, continues along the coast of Oman, and after an eastward meandering joins the southward undercurrent along Somalia. This result is in agreement with a numerical solution of Semtner and Chervin (1992), analyzed by Schott and Fischer (2000) for the Arabian Sea. Results of another OGCM (Anderson et al., 1991) demonstrate existence of an onshore surface flow between 7°N and 10°N. A similar westward current, which supplies some water for the winter Somali Current, exists in MKM. As in the present solution, a southward Somali Undercurrent in MKM is fed by a westward flow across the interior of the Arabian Sea. Signature of the higher-salinity Persian Gulf Water is clearly seen in Figs. 8 and 9 off Somalia during the Northeast Monsoon. Contribution to the coastal undercurrent mainly comes from the Gulf of Aden through the Socotra passage (Fig. 4a). Thus, coastal currents that form as a result of outflows of denser water from the Gulf of Aden and the Persian Gulf contribute to the winter coastal undercurrent.

5.2. Contribution from waves to the generation of the undercurrent

While the above analysis demonstrates that the flows from the north and northeast supply water for the undercurrent north of 5°N, previous studies

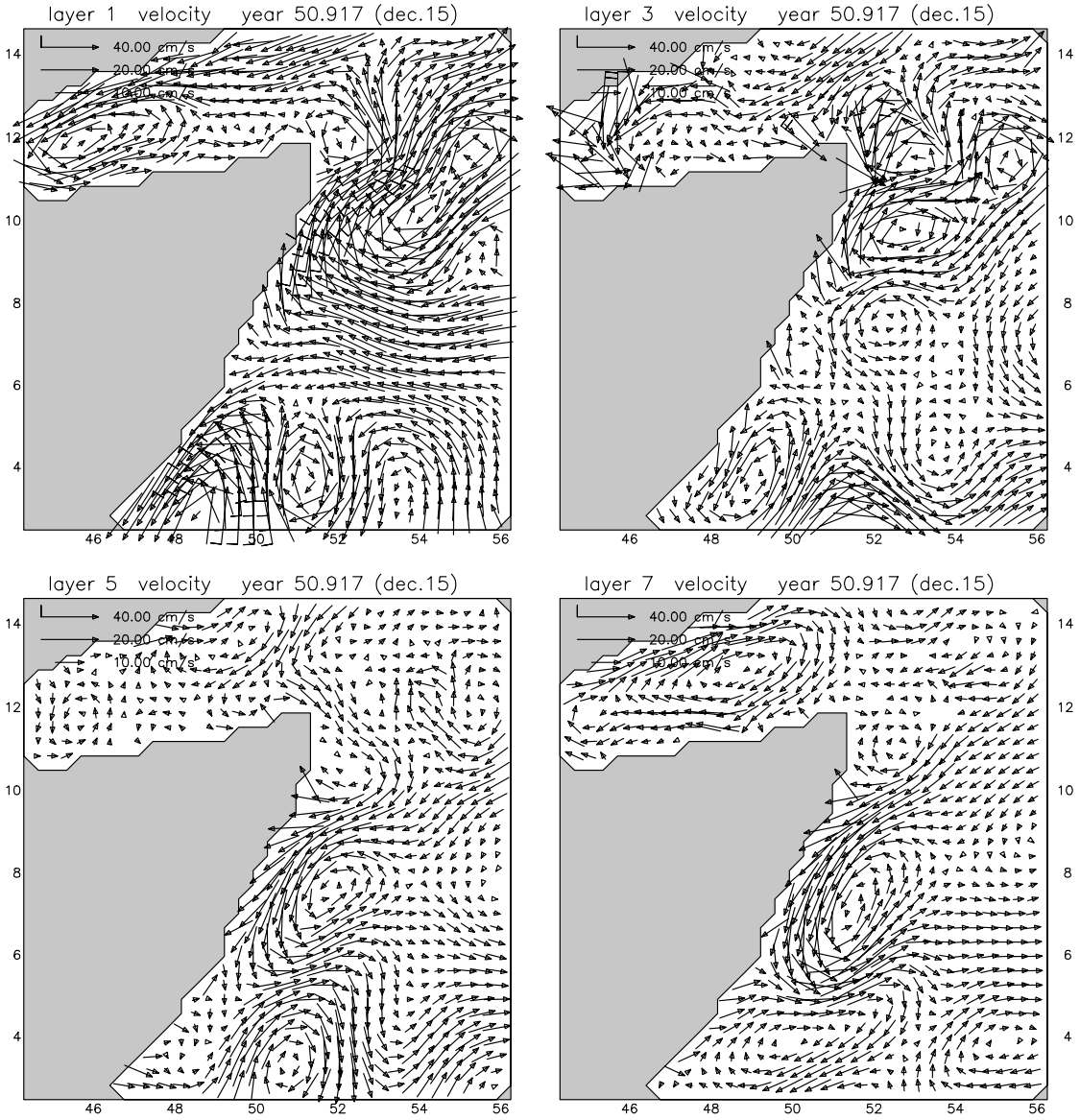

Fig. 12. Circulation in different layers in the model during the winter monsoon. Flows from the north and northeast contribute to the southward undercurrent.

(Jensen, 1991; MKM) show the importance of the Rossby waves in generating the undercurrent. To investigate effects of remote forcing on the evolution of the coastal undercurrent, a longitude-time plot of the thickness anomaly of layer six, which occupies depth range between 250 and 350 m and where the core of the coastal undercurrent is found, is calculated near 8°N. The largest values of the thickness anomaly in the coastal region off Somalia (Fig. 14) are caused by local winds and inflows from the interior of the domain. Formation of the Great Whirl is manifested by a broader region of elevated anomaly values near the coast in the summer. Fig. 14

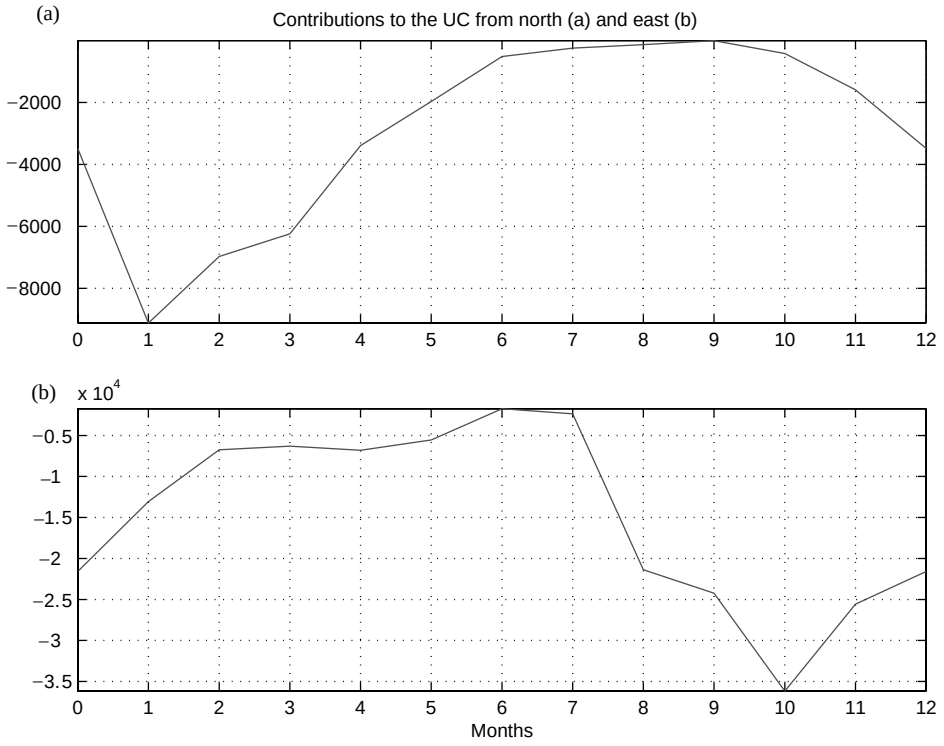

Fig. 13. Evolution of transports contributing to the winter Somali undercurrent from the north across 11°N (a) and from the east across 54°E (b). Only southward and westward components are used in the calculations.

demonstrates that a Rossby wave forced by reversal of the winds in the interior of the domain in late fall, propagates westward, and reaches the coastal region in October. At this time the summer monsoon subsurface circulation, dominated by the Great Whirl, weakens and the undercurrent appears. The wave carries a thickness anomaly with an amplitude of 10 m and has a larger zonal wavelength than width of the undercurrent. The phase speed of this wave (about 3.3 cm/s) is slightly less than the phase speed of mode-3 annual Rossby wave (5 cm/s), which dominates Jensen's (1991) solution.

Estimating the terms in the energy equation in the coastal region near 8°N demonstrates that remote forcing accounts for about 20% of the total energy change in the area during the fall. A time series of the thickness anomaly at 57°E, 8°N clearly demonstrates propagation of this wave, with the largest layer six thickness values observed in May and June (Fig. 15). Spectral analysis of this signal reveals that the annual component dominates. It should be noted here that higher-frequency signals are not present in this plot due to a limited temporal sampling of the model results (every 30 days). These signals cannot be directly forced by the climatological monthly forcing used in the model, and may be caused by instabilities. To summarize, contribution of the annual Rossby wave, which originates in the interior of the domain in winter and reaches the Somali coast in October, accounts only for about 20% of the total energy change in the region near 8°N.

6. Effects of bottom topography and wind forcing on the subsurface coastal circulation

One of the advantages of the MICOM is that it includes interaction of currents with bottom

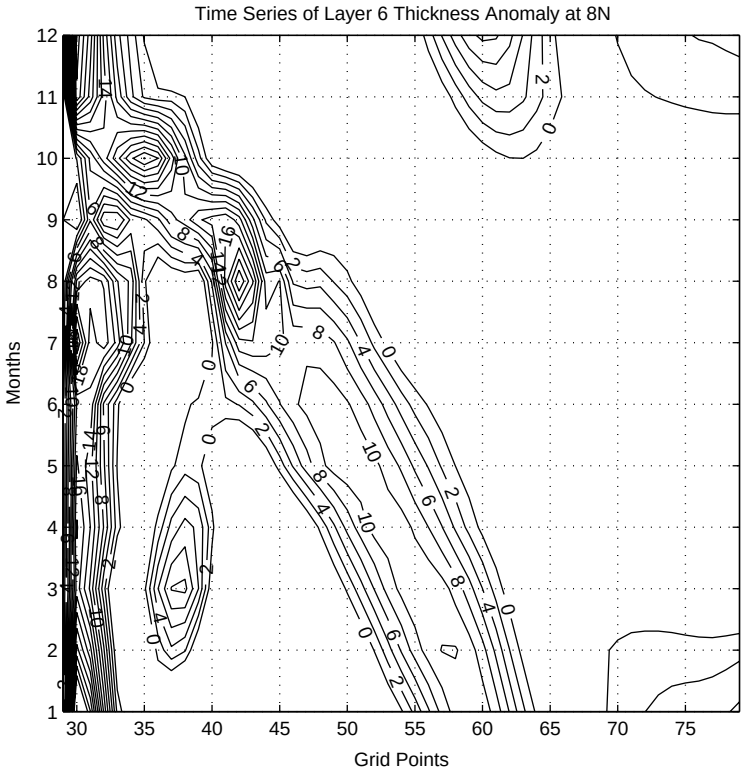

Fig. 14. Annual cycle of the model layer 6 (which corresponds to about 200–300 m depth range) thickness anomaly near 8°N. The largest values of the anomaly are found in the nearshore region. The annual mean thickness of the layer is 102 m, with amplitude 4 m. Propagation of the wave from the interior coincides with reestablishment of the coastal undercurrent in October.

topography, which is missing in the previously used reduced-gravity models. Effects of topography and variable wind forcing on the subsurface circulation near the coast of Somalia are the subject of this section.

6.1. Influence of the Socotra Island

The Socotra Island is submerged under about 300 m of water in the model due to a limited horizontal resolution. The island may have some impact on the subsurface circulation off Somalia because there are rather strong flows above the submerged island in the model. To study how presence of the island changes the summer circulation, an experiment was performed with the model bottom topography modified in such a way that grid points off the tip of Somalia with depth values less than 400 m were replaced by land points. As a result, the model island appears approximately in the location of the real one.

Comparison of the results of the current experiment with the standard solution shows that flow patterns below the surface are essentially the same in both cases in winter, except that the southward flow north of 5°N is slightly stronger and the coastal current from the south is found farther offshore in the former case (Figs. 16a and 4a). Significant differences between the two runs appear during the spring transition period (Figs. 16b and 4b). In the standard case the southward undercurrent associated with an onshore flow at 5°N exists only south of this latitude. When the Socotra Island is present, another spring undercurrent appears between 10°N and 5°N, which has been documented by Schott et al.

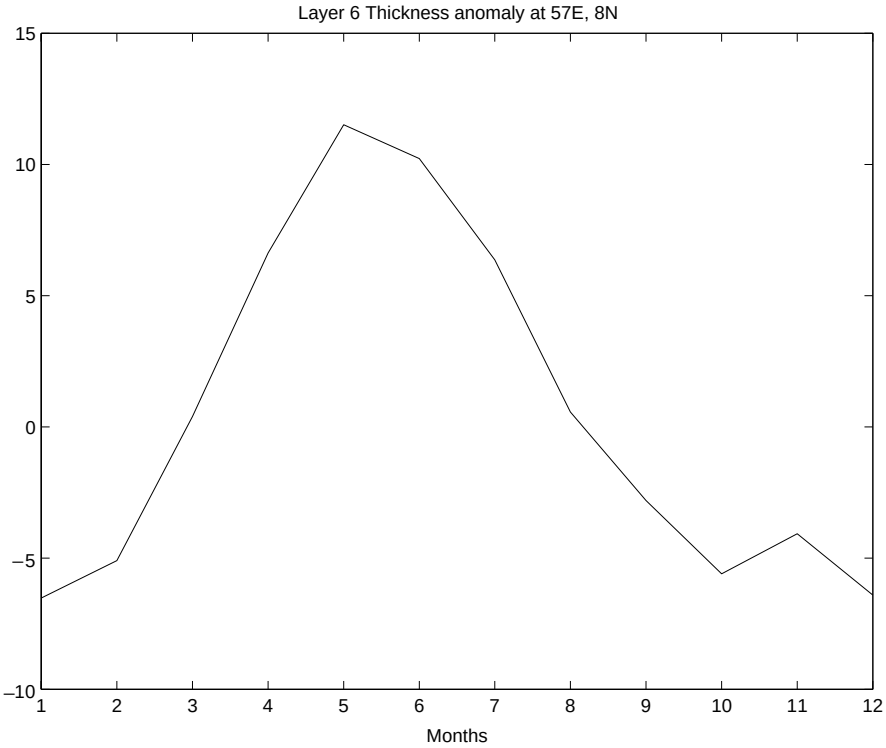

Fig. 15. Time series of layer 6 (200–300 m depth range) thickness anomaly at 57°E, 8°N. Maximum value occurs in May.

(1990, Fig. 2 in this study). Circulation in the rest of the domain is essentially unaffected. Summer circulation at mid-depth, dominated by the double-gyre system, is not influenced by the presence of the Island except in its close vicinity. Solutions of the two models are very similar during the rest of the year. Comparison of time series of the nearshore flow in the upper 800 m at 7°N in the present experiment (Fig. 17) with that in the standard simulation (Fig. 10b) leads to a similar conclusion. The coastal undercurrent lasts through May in the former case, while there is no undercurrent in spring in the standard experiment.

To summarize, presence of the Socotra Island in the model (rather than as a seamount) has a noticeable impact on the character of the coastal undercurrent during the spring transition period. Because observations show existence of the undercurrent near the northern part of the Somali coast at this time (QS), presence of the island is essential for a more realistic simulation of subsurface circulation in the region.

6.2. Impact of coastal topography on the undercurrent

Schott (1983) suggests that the offshore separation of the undercurrent can be caused by interaction of the flow with a topographic bump near 4°N, where isobaths below 1000 m run almost zonally for about 100 km and then turn abruptly north. Fig. 18 demonstrates a significant excursion in the offshore direction of isobaths deeper than about 1000 m in the model. To test Schott's (1983) hypothesis, an experiment is performed with bottom depths less than 2000 m near the coast replaced with the 2000 m value.

There are no significant changes in the resulting flow pattern in the undercurrent depth range. Analysis of a time series of coastal currents reveals that at 3.5°N, south of the topographic feature, a

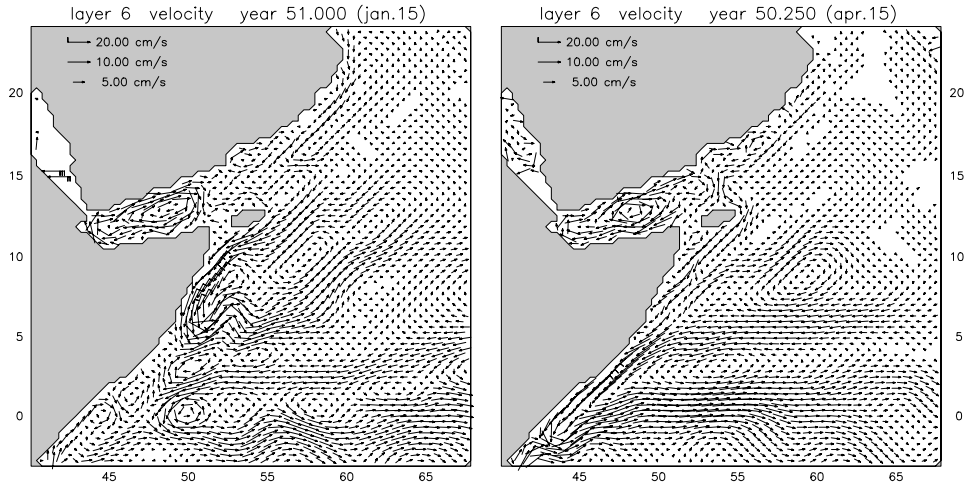

Fig. 16. Seasonal cycle of circulation in the presence of the Socotra Island in the depth range between 200 and 300 m. The undercurrent in the present experiment exists throughout the spring and extends farther north than in the standard run.

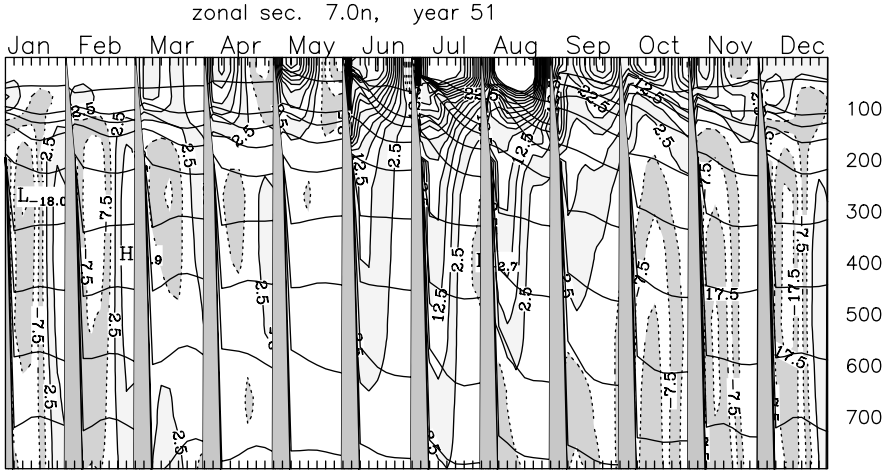

Fig. 17. Evolution of coastal circulation at 7°N in the presence of the Socotra Island. The undercurrent is present in April and early May, in contrast to the standard case.

southward undercurrent is stronger in October, November and December than that in the standard experiment (cf. Figs. 19 and 10d, largest velocity 9–11 vs 4–5 cm/s). The northward flow below 100 m weakens in the present experiment, and even a countercurrent appears farther offshore in January. This tendency continues into late winter, when the northward flow between 150 and 300 m disappears. Time series of the model alongshore transport confirms the above analysis. Even though the southward current reaches 4°N in the present case in late winter, about one degree farther south than in the standard run (cf. Figs. 20 and 5), differences between the two experiments are not significant during the rest of the year.

6.3. Variability of circulation under observed wind forcing

While strong interannual variability of surface circulation was observed in the Arabian Sea (S83), existing data do not allow evaluation of the deeper

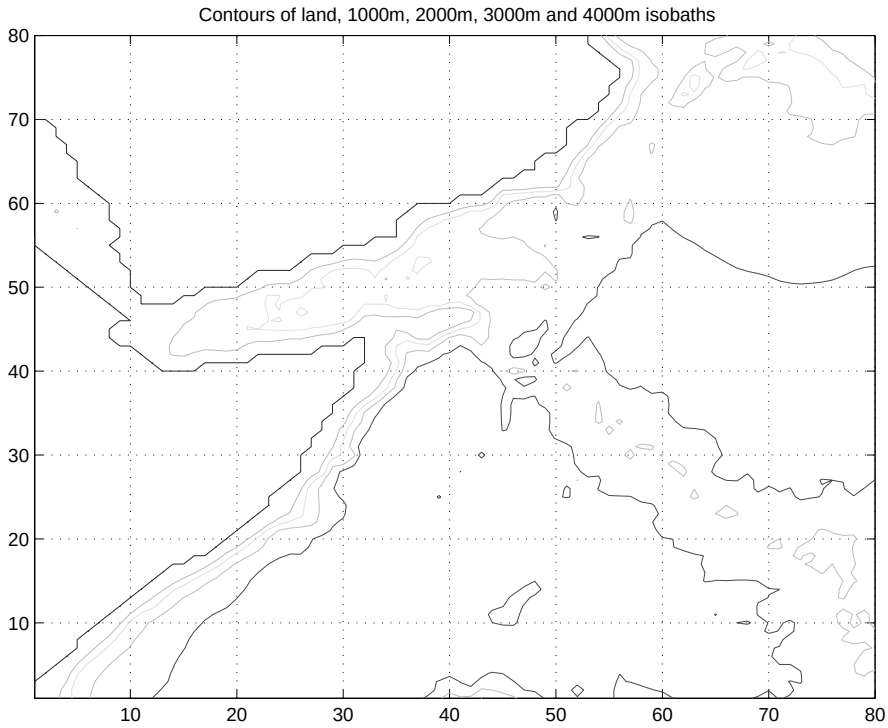

Fig. 18. Model bottom topography. Contours of land, 1000, 2000, 3000 and 4000 m depth are shown. Axes are labeled with grid point indices.

circulation variability. Luther and O'Brien (1989) used a $1\frac{1}{2}$-layer model to show that interannual variability of surface circulation increases significantly when observed, rather than climatological, wind forcing is used. Improved vertical resolution in MICOM allows us to study effects of the observed winds on circulation below the surface. For this purpose, standard deviations of velocities in the undercurrent depth range in a simulation forced with the FSU wind product (Legler et al., 1989) are compared with those in the standard run. The largest variability is found in the coastal region and near the Socotra Island in both simulations. Results of the current experiment demonstrate stronger variability over a larger region than in the standard simulation in winter (Fig. 21). The differences between the two cases increase dramatically during the summer monsoon (Fig. 22). As expected, the standard deviations of velocity are found in the area where the two deep-reaching eddies consistently form, and thus can be attributed to interannual variability of their strengths and positions. The region of the highest values of velocity variability occupies a larger area of the domain in the present simulation with the strongest velocities by a factor of three larger than those in the standard run.

Results of this study extend the conclusions of Luther and O'Brien (1989) to the deeper circulation. It is shown that interannual variability of subsurface fields increases dramatically when observed, rather than climatological, winds force the model. Conclusions for velocity apply to the other model variables because advection plays the primary role in their distribution under climatological thermodynamic forcing used in the model.

7. Conclusions

An eddy-resolving open boundary version of the MICOM is used to investigate subsurface circula-

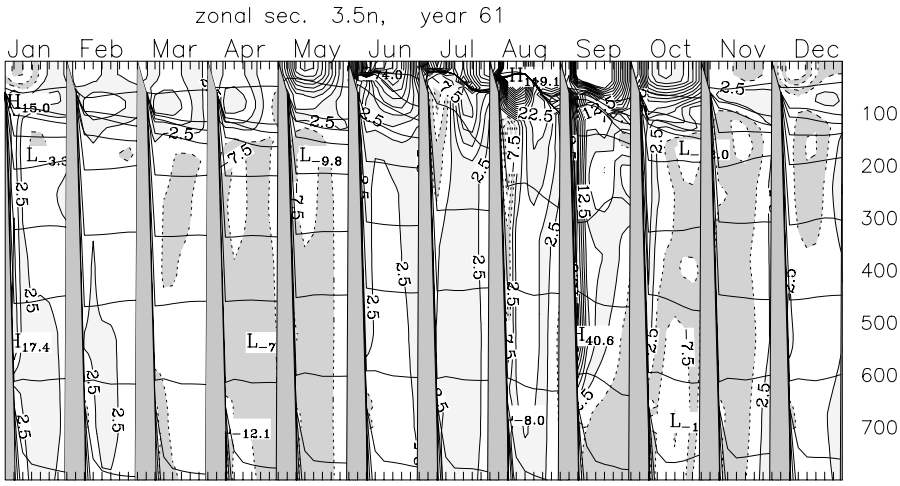

Fig. 19. Evolution of coastal circulation at 3.5°N in a simulation with bottom depths <2000 m replaced with a 2000 m value. The

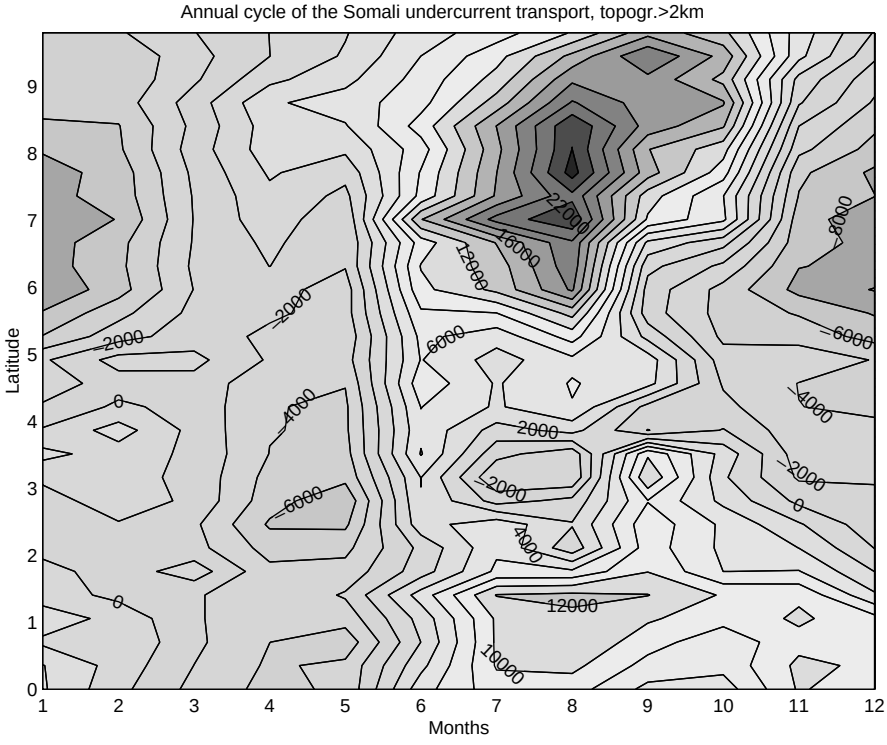

Fig. 20. Annual cycle of subsurface transport between the equator and 10°N in the simulation with bathymetry <2000 m removed.

tion and water masses in the western Arabian Sea. The model vertical resolution of the upper thermocline with 7 layers in the top 400 m is sufficient for the present study. Solutions demonstrate a strong annual cycle and significant alongshore variability of subsurface circulation. Based on dynamics and water properties, three regions are identified along the coast: (i) An

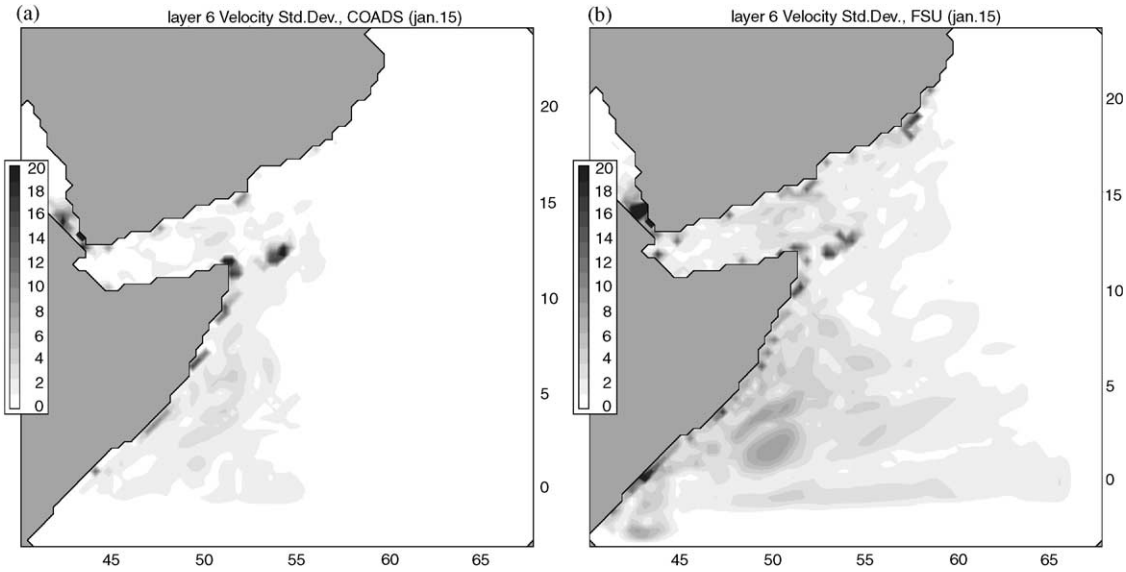

Fig. 21. Standard deviation of velocity at the undercurrent depth range in January (a) in the standard simulation forced with the COADS winds and (b) in a run forced with the FSU wind product.

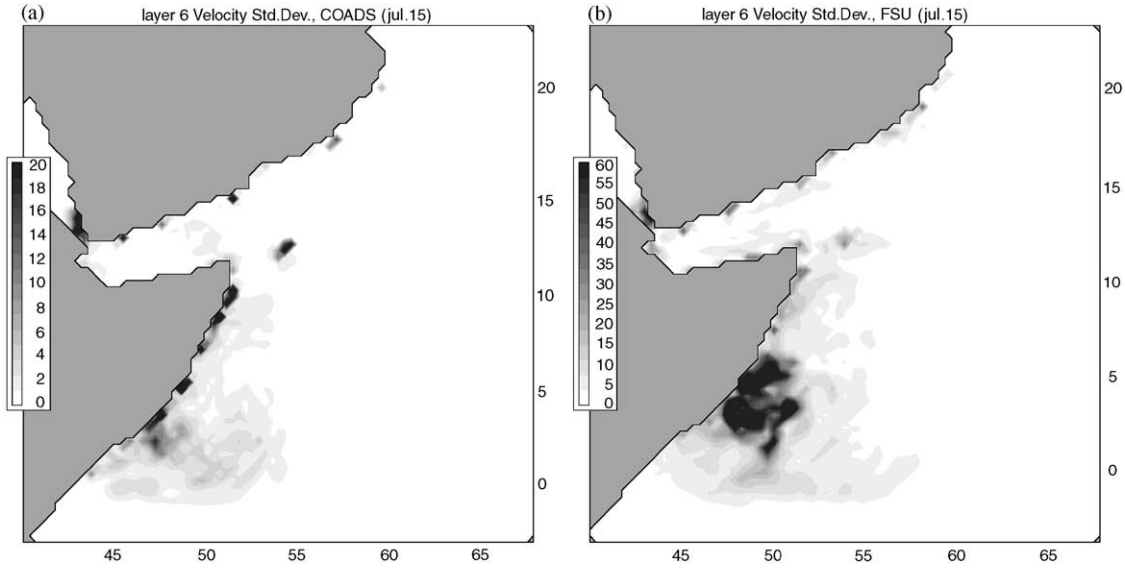

Fig. 22. Same as Fig. 21 but for July.

undercurrent north of 5°N, which transports high-salinity water southwards, is present between October and March. (ii) A cross-equatorial flow carries water with low salinity northwards. It exists throughout the year, peaks during the Southwest Monsoon, and reaches as far north as 3°N. A spring southward undercurrent between 5°N and the equator owes its existence to the wind forcing in the Arabian Sea. (iii) The southward undercurrent separates in an area around 4°N, as velocity and salinity fields demonstrate in winter and spring. The three undercurrents discussed in this study also were found in solutions of MKM. The modeled and observed annual cycles of

subsurface circulation and transport are in close agreement near the equator, where consistent observations exist. However, the model cross-equatorial flow is shallower than in the observations, and velocity in the core of the current is underestimated by about a factor of 2. This limitation is reduced when the model horizontal resolution is increased from 0.35° to 0.225°.

Existence of the winter undercurrent north of 5°N is primarily due to subsurface flows from the north and northeast. The current from the northeast dominates and carries higher-salinity water from the Persian Gulf. Another contribution comes from the annual Rossby wave generated in the interior of the domain in winter, which accounts for about 20% of total energy change at the time of the undercurrent formation.

To test Schott's (1983) hypothesis that separation of the southward undercurrent is caused by its interaction with a topographic ridge near 4°N, an experiment is performed where bottom depths less than 2000 m off Somalia are replaced with a 2000 m value. This modification leads to slight changes in subsurface circulation only near the ridge, implying that model solutions are not sensitive to the details of bottom topography in the region. On the other hand, presence of the Socotra Island, which is not resolved in the standard simulation, leads to closer agreement with the observations. In this case, the model undercurrent north of 5°N exists during spring in contrast to the standard simulation.

When forced with observed winds (the FSU wind product), interannual variability of subsurface fields off the Somali coast and near the equator increases significantly, especially during the summer monsoon in the region where the deep-reaching eddies form. This result is an extension to the deeper circulation of conclusion obtained with a $1\frac{1}{2}$-layer model by Luther and O'Brien (1989).

Acknowledgements

The authors want to thank Dr. Rainer Bleck for providing the numerical model and for his advice during the course of this study. Special thanks are due to Fritz Schott and Julian P. McCreary, Jr. whose valuable suggestions improved the work. Part of this study was supported by NSF OCE-9314447 Grant.

References

Anderson, D.L.T., Carrington, D.J., Corry, R., Gordon, C., 1991. Modeling the variability of the Somali Current. Journal of Marine Research 49, 659–696.

Bleck, R., Rooth, C., Hu, D., Smith, L.T., 1992. Salinity-driven thermocline transients in a wind- and thermohaline-forced isopycnic coordinate model of the North Atlantic. Journal of Physical Oceanography 22, 1486–1505.

Brock, J.C., McClain, C.R., 1992. Interannual variability in phytoplankton blooms observed in the northwestern Arabian Sea during the Southwest Monsoon. Journal of Geophysical Research 97, 733–750.

Browning, G.L., Kreiss, H.-O., 1982. Initialization of the shallow water equations with open boundaries by the bounded derivative method. Tellus 34, 334–351.

Browning, G.L., Kreiss, H.-O., 1986. Scaling and computation of smooth atmospheric motions. Tellus 38A, 295–313.

Duing, W., Schott, F., 1978. Measurements in the source region of the Somali Current during the monsoon reversal. Journal of Physical Oceanography 8, 278–289.

Godfrey, J.S., Alexiou, A., Ilahude, A.G., Legler, D.M., Luther, M.E., McCreary, J.P., Meyers, G.A., Mizuno, K., Rao, R.R., Shetye, S.R., Toole, J.H., Wacongne, S., 1995. The role of the Indian Ocean in the global climate system: recommendations regarding the global ocean observing system. Ocean Observing System Development Panel Report, Texas AM University, College Station, TX, 89pp.

Hurlburt, H.E., Thompson, D.D., 1976. A numerical model of the Somali Current. Journal of Physical Oceanography 6, 646–664.

Jensen, T.G., 1991. Modeling the seasonal undercurrents in the Somali current system. Journal of Geophysical Research 96, 22,151–22,167.

Kraus, E.B., Turner, J.S., 1967. A one-dimensional model of the seasonal thermocline. Part II: The general theory and its consequences. Tellus 19, 98–106.

Luther, M.E., O'Brien, J.J., 1989. Modelling the variability in the Somali Current. In: Nihoul, J.C., Jamart, B.M. (Eds.), Mesoscale/Synoptic Coherent Structures in Geophysical Turbulence. Elsevier, New York, pp. 373–386.

McCreary, J.P., Kundu, P.K., 1985. Western boundary circulation driven by an alongshore wind: with application to the Somali Current system. Journal of Marine Research 43, 493–516.

McCreary, J.P., Kundu, P.K., 1988. A numerical investigation of the Somali Current during the Southwest Monsoon. Journal of Marine Research 46, 25–58.

McCreary, J.P., Kundu, P.K., Molinari, R.L., 1993. A numerical investigation of dynamics, thermodynamics and

mixed-layer processes in the Indian Ocean. Progress in Oceanography 31, 181–244.

McCreary, J.P., Kohler, K.E., Hood, R.R., Olson, D.B., 1996. A four-component ecosystem model of biological activity in the Arabian Sea. Progress in Oceanography 37, 193–240.

Quadfasel, D.R., Schott, F., 1983. Southward subsurface flow below the Somali Current. Journal of Geophysical Research 88 (C10), 5973–5979.

Schott, F., 1983. Monsoon response of the Somali Current and associated upwelling. Progress in Oceanography 12, 357–381.

Schott, F., Swallow, J.C., Fieux, M., 1990. The Somali Current at the equator: annual cycle of currents and transports in the upper 1000 m and connection to neighboring latitudes. Deep Sea Research 37, 1825–1848.

Schott, F., Fischer, J., 2000. The winter monsoon circulation of the northern Arabian Sea and Somali Current. Journal of Geophysical Research 105, 6359–6376.

Semtner, A.J., Chervin, R.M., 1992. Ocean general circulation from a global eddy-resolving model. Journal of Geophysical Research 97, 5493–5550.

Wacongne, S., Pacanowski, R.C., 1995. Seasonal heat transport in a primitive equations model of the tropical Indian Ocean. Journal of Physical Oceanography 26, 2666–2699.